PCCP

PAPER

Cite this: *Phys. Chem. Chem. Phys.*, 2022, **24**, 17337

The Zintl phase compounds $AEIn_2As_2$ (AE = Ca, Sr, Ba): topological phase transition under pressure†

Wen-Ti Guo, [ab] Zhigao Huang [ab] and Jian-Min Zhang *[ab]

Received 16th April 2022,
Accepted 27th June 2022

DOI: 10.1039/d2cp01764d

rsc.li/pccp

$AEIn_2As_2$ (AE = Ca, Sr, Ba), as a new crucial nonmagnetic thermoelectric candidate, needs to be understood in terms of its potential electronic structure properties and topological characteristics in both experimental and theoretical studies. Here we report that $AEIn_2As_2$ with Zintl phases will undergo insulator–metal phase transition and topological quantum phase transition under pressure modulation based on first-principles calculations. Firstly, band inversion occurred between the In(As)-s and As(In)-p states in the structures of $AEIn_2As_2$ with the $P6_3/mmc$ space group in the absence of pressure and identified that they are all non-trivial topological insulators. Next, Bader charge and AIM topology analysis elucidate the nature of pressure-induced chemical bond enhancement. Lastly, we have discovered pressure-controllable band gap closure while the topologically protected surface states disappear, realizing insulator–metal phase transition and topological quantum phase transition. Our research not only enriches the family of topological insulators but also provides a good platform for the study of thermoelectric properties.

1 Introduction

In recent years, EuX_2As_2 (X = Cd, In, Sn) have been of great interest in the field of condensed matter physics due to their intrinsically novel physical properties. As a typical Dirac semimetal,[1–3] $EuCd_2As_2$ can be topologically phase transformed by applying pressure[1] or electric field[4] to adjust the direction of the magnetic moment, and the Weyl semimetal state induced by spin fluctuation is observed in its paramagnetic state.[5] It has also been studied that $EuCd_2As_2$ with different magnetic orders for possible an axion insulator, AFM topological crystal insulator, or higher-order topological insulator.[6] $EuIn_2As_2$ is reported to have higher order topological insulator and axion insulator features.[7–11] At the same time, the topological phase transition can be induced by adjusting the magnetic configuration of $EuIn_2As_2$.[10–12] A new magnetic topological insulator, $EuSn_2P_2$, has been designed.[13] $EuSn_2As_2$, which was first reported as having a layered structure with a peelable Zintl–Klemm phase,[14] was later shown theoretically and experimentally to be an intrinsically magnetic topological insulator.[15] Recent results show that $EuSn_2As_2$ can undergo a phase transition from $R\bar{3}m$ symmetry to $C2/m$ symmetry under high pressure above ~14 GPa[16] and a new high-pressure rhombohedral phase was found at 15 GPa.[17] The series of compounds EuX_2As_2 (X = Cd, In, Sn) are all considered to have the potential to be regulated and to undergo a topological phase transition.[1,4,10–12,16]

Notably, the topological quantum phase transitions obtained from the non-magnetic novel structures of alkaline earth (AE) metal substituted Eu positions are reflected in both $Sr(Ba)Cd_2As_2$[21–23] and $SrSn_2As_2$.[24,25] It proposes that the Zintl $CaAl_2Si_2$ type material CaM_2Bi_2 (M = Zn or Cd) is a topological insulator.[26] The AM_2X_2 (A = Ca, Sr, or Ba; M = Zn or Cd; X = Sb or Bi) series of materials were confirmed as topological insulators with band inversion and the coexistence of insulating topological state and the Rashba effect in the $BaCd_2SbBi$ film was achieved.[27] Inspired by SrX_2As_2 (X = Cd, Sn) non-magnetic materials, we propose the new idea that $AEIn_2As_2$ (AE = Ca, Sr, Ba) topological insulators may also undergo topological quantum phase transitions or metal–insulator phase transitions. A recent report confirmed our conjecture, which shows that $BaIn_2As_2$ is a typical degenerate p-type semiconductor, but it does not attain the electrical and transport properties of $CaIn_2As_2$ and $SrIn_2As_2$.[18] The $AEIn_2As_2$ family, which belongs to the Zintl phase, is fresh and full of mysterious narrow-band semiconductor materials, which have stimulated a wide range of theoretical and experimental research interests. Zintl phase compounds consisting of closed-shell electron configuration elements are a class of polar intermetallic compounds. The important narrow band gap properties and excellent thermoelectric characteristics prompt their use as candidates for thermoelectric materials. However,

[a] *Fujian Provincial Key Laboratory of Quantum Manipulation and New Energy Materials, College of Physics and Energy, Fujian Normal University, Fuzhou 350117, China. E-mail: jmzhang@fjnu.edu.cn*

[b] *Fujian Provincial Collaborative Innovation Center for Advanced High-Field Superconducting Materials and Engineering, Fuzhou, 350117, China*

† Electronic supplementary information (ESI) available. See DOI: https://doi.org/10.1039/d2cp01764d

the exploration of the electronic structures and topological properties of $AEIn_2As_2$ is urgent.

External regulation (pressure or external electric field) usually plays a crucial role along with the process of studying topological quantum phase transitions. The electronic structures of Bi_2Te_2Se and Bi_2Se_2Te films exhibit robustness to electric fields.[28] The topological phase transition was induced by applying hydrostatic pressure to $MnBi_2Te_4$ by Pei *et al.*[29] Mutch *et al.* found the essential basis for the pressure-tuned $ZrTe_5$ topological phase transition.[30] Pressure-induced topological phase transition was also confirmed in the Dirac semimetal Cd_3As_2.[31,32] In a word, due to its low cost and ease of operation, external pressure is widely used in experimental studies. And the introduction of pressure often leads to interesting and important potential properties, such as thermoelectric performance control,[33] structural phase transition,[29,34–37] metal–insulator phase transitions with band gap changes[38–41] and topological phase transitions with band inversion.[29–32,42–47]

Obviously, as a novel material, many physical properties of $AEIn_2As_2$ (AE = Ca, Sr, Ba) are not yet known. With reference to the results of theoretical and experimental studies, SrX_2As_2 (X = Cd, Sn) have a narrow band gap characteristic that is easily modulated by the external field.[22,24] In this study, we report the discovery of topological phase transition and metal–insulator phase transition in $AEIn_2As_2$ induced *via* pressure. At atmospheric pressure, $AEIn_2As_2$ systems are capable of band inversion phenomena, symbolizing non-trivial topological properties. Under the modulation of external pressure, they will undergo insulator–metal phase transition and topological quantum phase transition. $AEIn_2As_2$ as a new topological insulator deserves further study, and its unique surface state structure has important inspirations and applications for the practical production of electronic devices in this field.

2 Crystal structure and calculation methods

Our first-principles density functional theory calculations are implemented in the Vienna *ab initio* simulation package (VASP)[48,49] by using projected augmented wave (PAW)[50] and Perdew–Burke–Ernzerhof (PBE) type generalized gradient approximation (GGA)[51] exchange–correlation function and the hybrid functional HSE06.[52] The energy cutoff of the plane wave basis set is set to 400 eV, and the s semi-core orbital of the AE atom is considered as a valence electron. All the calculations that we focus on took into account spin–orbit coupling (SOC). Fig. 1(a) and (b) show the structure of $AEIn_2As_2$, which belongs

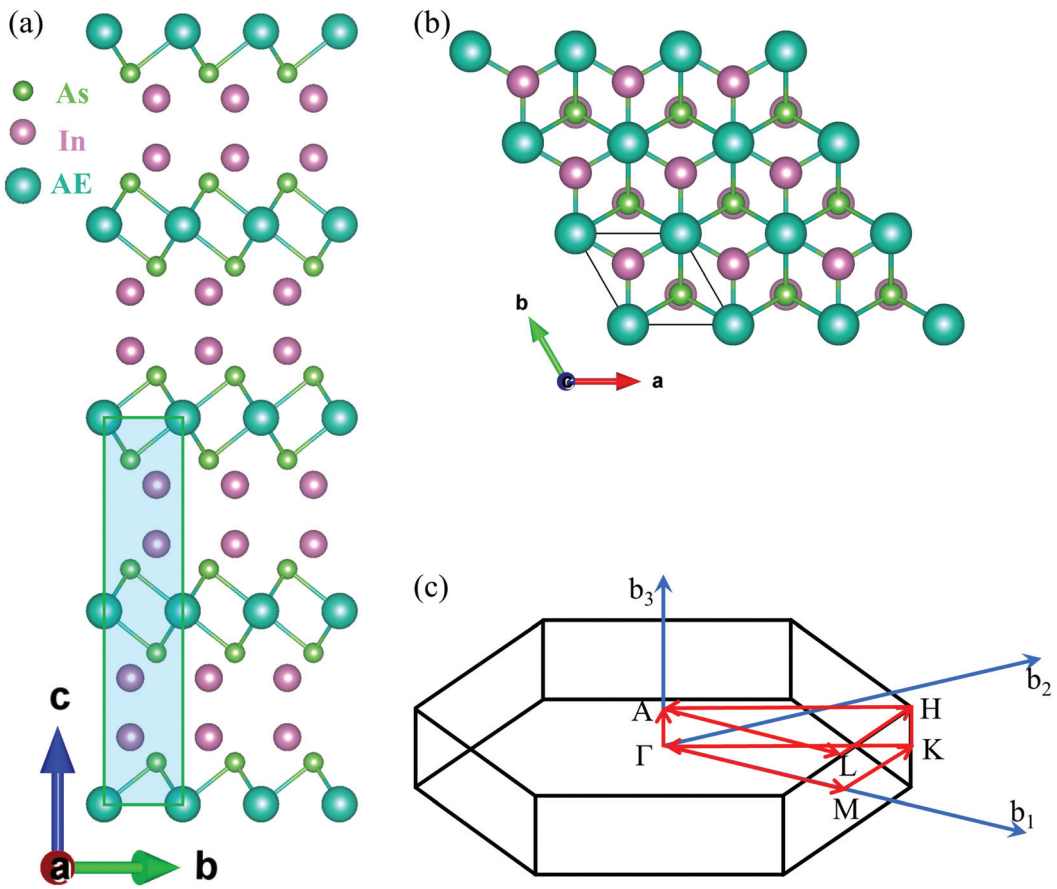

Fig. 1 The (a) side view and (b) top view crystal structures of $AEIn_2As_2$ with the $P6_3/mmc$ space group. (c) Its corresponding first Brillouin zone paths, which contain all high-symmetry points. The unit-cell structure is highlighted in green color shading in 1(a).

to the space group $P6_3/mmc$ (No. 194). First Brillouin zone is also shown in Fig. 1(c). The specific lattice constants of each material are presented in Table 1. The Γ-centered Monkhorst–Pack k-point mesh is considered as $11 \times 11 \times 3$. The absolute magnitude of the force on each atom is reduced below 0.02 eV $Å^{-1}$ for the ionic relaxation in our all calculations. The CP2K quantum chemistry and solid-state physics package[53] based on the hybridized generalized PBE0 combined with the DZVP-MOLOPT-SR-GTH basis group is applied to $AEIn_2As_2$ for single-point energy calculations to obtain the wave function files needed for topological analysis. The Multiwfn Multifunctional Wavefunction Analyzer[54] is used to perform Atoms in Molecules (AIM)[55,56] theoretical analysis of the calculated chemical bonds. To reproduce the band structure, a tight-binding model based on Maximum Local Wannier Functions (MLWFs)[57,58] was constructed. Then based on the surface Green's function approach,[59–62] the calculations of Wannier Charge Center (WCC), surface states, and Fermi surfaces (FS) of the semi-infinite surfaces were implemented using the Wannier-Tools package.[63]

3 Results and discussion

In this section, we systematically investigated the insulator–metal phase transition and topological phase transition of $AEIn_2As_2$ under pressure induction. Firstly, we study the bulk modulus and electronic structure of $AEIn_2As_2$ under high pressure in Section 3.1 to reveal the intrinsic mechanism of insulator–metal phase transition. Section 3.2 reveals the charge transfer and chemical bonding nature of the systems under pressure. Section 3.3 performs surface state and WCC calculations for $AEIn_2As_2$ possessing $P6_3/mmc$ space group to demonstrate the pressure-induced topological phase transition.

3.1 Electronic structures and bulk properties

To study the electronic structure of the three $AEIn_2As_2$ systems, we calculated their band structures under different pressures (see Fig. S1 and S2, ESI†) and compare the results for the PBE and HSE06 calculations of $BaIn_2As_2$ in Fig. 2. In the absence of pressure, both HSE06 and PBE give a band gap of approximately 0.1 eV. The band gap results obtained from the HSE06 calculations are smaller than the PBE under low-pressure action (below 8 GPa). However, PBE results slightly underestimate the global band gap after higher pressure action ($\geq$8 GPa). An intuitive comparison of the calculations of the two methods, PBE (blue curve in Fig. 3(b)) and HSE06 (Fig. 3(c)), reveals that they inevitably differ ($\sim$0.3 eV difference at 8 GPa). However, like the PBE calculations, HSE06 calculations also confirm that the trend of the $BaIn_2As_2$ band gap with hydrostatic pressure is different from that of $CaIn_2As_2$ and $SrIn_2As_2$. All three $AEIn_2As_2$ systems have a pressure value (see Fig. 3(b)) that allows the band gap to approach zero for AE = Ca, Sr, and Ba of 2, 6, and 10 GPa, respectively. The band structures of the three systems by adjusting the pressure values to a band gap of exactly zero are shown in Fig. S1(l) (ESI†), and the pressure values which induced zero band gap for AE = Ca, Sr, and Ba are 3, 6.637, and 10.555 GPa, respectively. From their band structures, it can be clearly seen that the conduction band minimum (CBM) and valence band maximum (VBM) of the zero band gap systems are shifted to the Γ high-symmetry point.

We next focus on the band gap variation regular of the three $AEIn_2As_2$ systems under pressure modulation. For $CaIn_2As_2$ and $SrIn_2As_2$, the indirect band gap first decreases to zero at Γ and then reopens. On the contrary, the band gap of $BaIn_2As_2$ maintains the trend of continuous decrease due to the gradual drooping of the conduction band at the M high symmetry point. Unlike the indirect band gap near Γ that gradually shifts with pressure before the band gap closes, the local direct band gap at Γ is reopening and stably locked at Γ after the pressure is higher than the value that induced the zero band gaps. These assertions are observed in the band structures in Fig. 2 and the band gap evolution trend curves in Fig. 3(b) and (c). In particular, the band gap trend of $BaIn_2As_2$ is different from the other two because of the emergence of competing states in the conduction band with a gradual droop at the M-high symmetry point. From the local band gap curve at Γ of the $BaIn_2As_2$ system in Fig. 3(b), we can find that the band gap variation regular is similar to $CaIn_2As_2$ and $SrIn_2As_2$. Obviously, the band gap and electronic structure of the $AEIn_2As_2$ systems are very sensitive to pressure and possess the potential capability of pressure tunability.

In order to visually study the pressure-induced evolution regulation, we also quantitatively analyze the relevant physical parameters utilizing Table 1 and Fig. 3. The lattice parameters of our fully relaxed and the references are numerically close to

Table 1 Lattice constants of the three crystal structures, the band gaps, and the special values of pressure corresponding to the zero band gap P_c with the literature result comparison of our PBE calculations. The bulk modulus B_0 and its derivative B_1 were obtained by fitting the Birch–Murnaghan (B–M) equation according to the energy–volume curve under pressure modulation. The data sources are labeled in the upper right-hand corner, while those not labeled are the results of our PBE-based GGA calculations taking SOC into account

Crystal material	Space group	Lattice constants (Å)			Band gap (eV)	B_0 (GPa)	B_1	P_c (GPa)
		a	b	c				
$CaIn_2As_2$	$P6_3/mmc$	4.224, 4.148[a] 4.200[c]	4.224, 4.148[a] 4.200[c]	17.974, 17.726[a] 17.904[c]	0.06, 0.03[a], 0.20[c] 0.01[d]	46.3	4.38	3.000
$SrIn_2As_2$		4.307, 4.222[a] 4.324[b]	4.307, 4.222[a] 4.324[b]	18.356, 18.110[a] 18.272[b]	0.10, 0.03[a] 0.01[d]	43.8	4.47	6.637
$BaIn_2As_2$		4.394	4.394	18.831	0.11, 0.01[d]	41.7	4.50	10.555

[a] Ref. 18 (w/o SOC). [b] Ref. 19 (w/o SOC). [c] Ref. 20 (w/o SOC). [d] Our w/o SOC calculation.

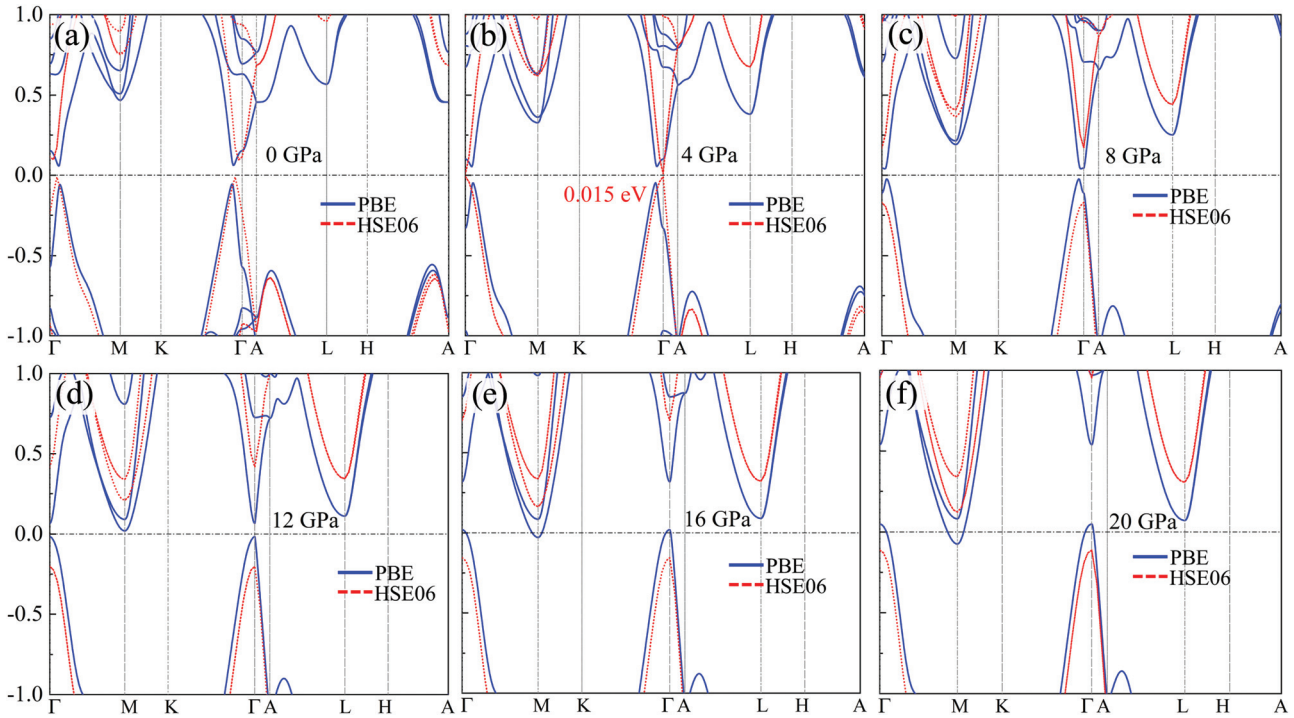

Fig. 2 (a)–(f) Band structure evolution diagrams of $BaIn_2As_2$ systems *via* PBE and HSE06 functionals under different hydrostatic pressures. The horizontal and vertical gray dashed lines indicate the Fermi level and the high symmetry line.

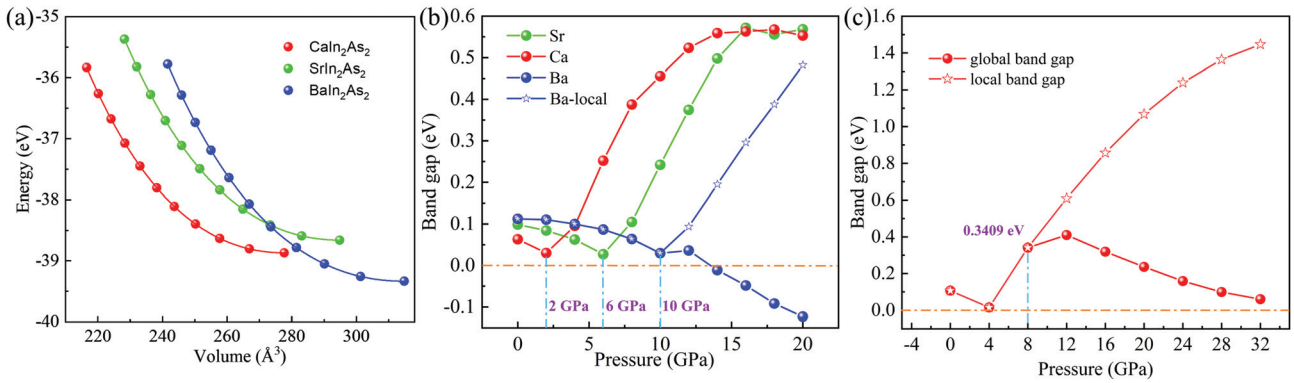

Fig. 3 (a) Energy–volume curves fitted using the Birch–Murnaghan (B–M) equation for the three $AEIn_2As_2$ systems under different hydrostatic pressures. (b) Evolutionary regular curves of $AEIn_2As_2$ of the band gap by PBE calculation using hydrostatic pressure. (c) The band gap *vs.* pressure curves of $BaIn_2As_2$ under HSE06 calculation with hydrostatic pressure. The hollow pentagons in (b) and (c) indicate the local band gap at the vicinity of the Γ point.

each other and are given in Table 1. The corresponding evolution curves of lattice constant $a(b)$, and lattice constant c of $AEIn_2As_2$ under hydrostatic pressure are shown in Fig. S2(a) and (b) (ESI†). For comparison with literature calculations for the SOC absence, we calculated the band gap without SOC, given by the data marked with d in the upper right corner of Table 1. Due to the difference in lattice constants and calculation methods, our calculations in the absence of SOC action are smaller than the results in the literature, but this does not delay our study of the band gap variation dependence regular on pressure. The specific band gap values at atmospheric pressure containing SOC are also presented in Table 1, corresponding AE = Ca, Sr, and Ba are 0.06 eV, 0.10 eV, and 0.11 eV, respectively. As with $AECd_2As_2$,[22] the lattice constants of $AEIn_2As_2$ all increase with the atomic radius of the AE atom. However, it can be seen in Fig. 3(b), that in contrast to the reported findings for $AECd_2As_2$,[22] the three $AEIn_2As_2$ systems show a monotonically increasing band gap in the AE series from Ca to Sr and Ba. As mentioned in the previous study,[22] the band gap should increase with the ionicity of the AE elements, and our calculation results just coincides with this feature.

Notably, as the blue vertical dashed–dotted lines shown in Fig. 3(b), all three $AEIn_2As_2$ systems have a critical pressure where the band gap is close to zero. By further calculations, as

illustrated by the P_c values in Table 1, the specific pressure value for band gap closure is reflected in all three $AEIn_2As_2$ systems, which also shows a positive correlation with the AE atomic radius. Obviously, in Fig. 3(b) and (c), comparing the band gap trends change with hydrostatic pressure for the three $AEIn_2As_2$ systems with $P6_3/mmc$ space group, we can find that $BaIn_2As_2$ shows very different results from $CaIn_2As_2$ and $SrIn_2As_2$, and this phenomenon is also reflected in the energy–volume curves in Fig. 3(a). The reason may be related to the chemical bonding between the material ions, which will be discussed further in the next section.

To study the bulk properties of $AEIn_2As_2$ under hydrostatic pressure, we have calculated total energy *versus* volume and fitted the curves to get the bulk modulus (B_0) and the derivative with respect to pressure (B_1) according to the Birch–Murnaghan (B–M), as shown in Fig. 3(c) and Table 1. The specific expression of the B–M equation[64] is shown as below:

$$E(V) = E_0 + \frac{9V_0B_0}{16}\left\{\left[\left(\frac{V_0}{V}\right)^{2/3}-1\right]^3 B_1 + \left[\left(\frac{V_0}{V}\right)^{2/3}-1\right]^2\left[6-4\left(\frac{V_0}{V}\right)^{2/3}\right]\right\} \quad (1)$$

where E_0 is the initial total energy, V_0 is equilibrium volume, B_0 is the bulk modulus, and B_1 is the derivative of B_0 with respect to pressure. The results of B_0 and B_1 about the three $AEIn_2As_2$ structures are shown in Table 1. It shows that the bulk modulus B_0 is getting smaller while its derivative B_1 is getting larger as the radius of the AE ion increases, indicating that the $BaIn_2As_2$ system is more unstable and more prone to structural phase

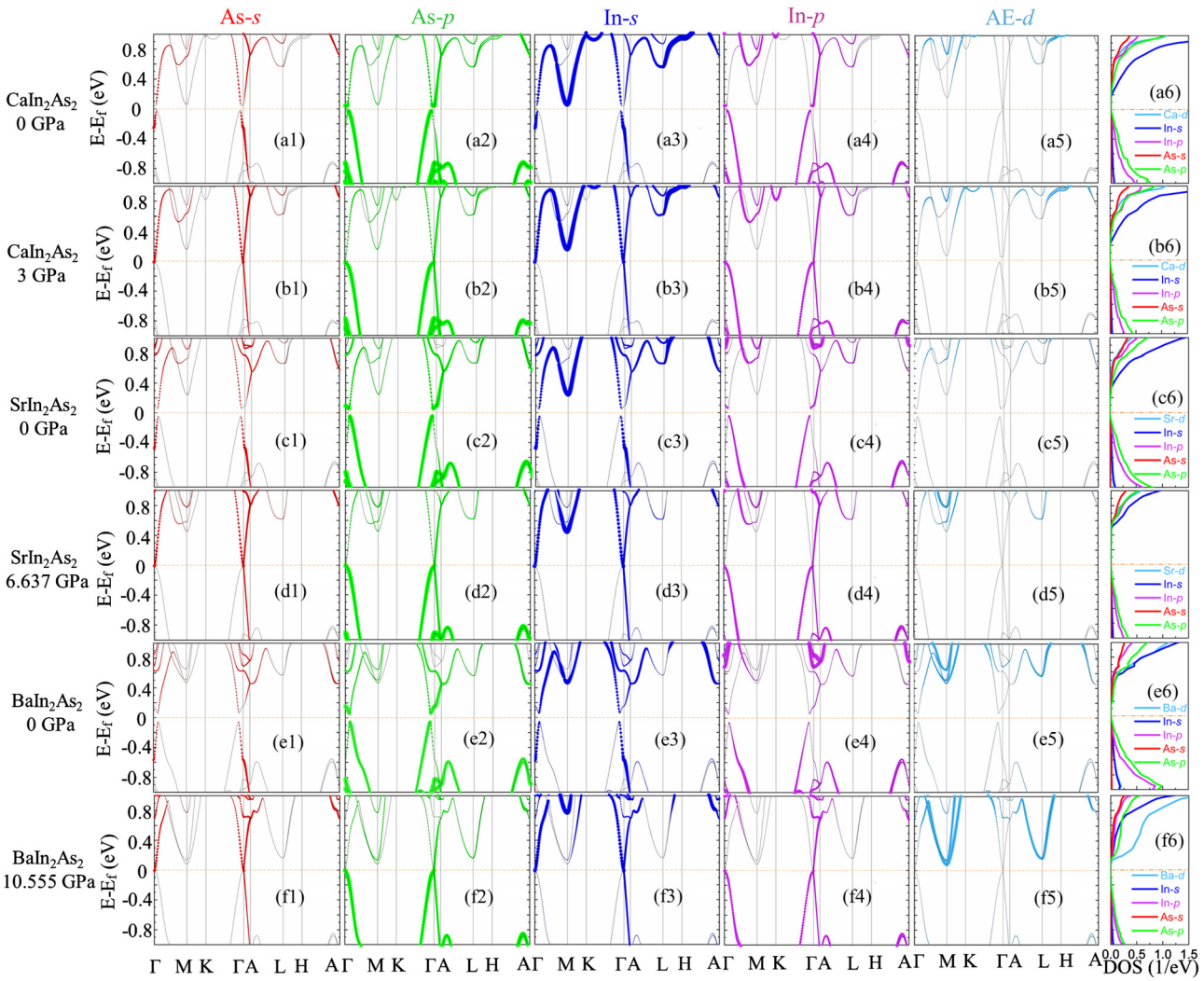

Fig. 4 Projection band structures together with their partial density of states of $AEIn_2As_2$ for the without pressure and the zero band gap pressure systems. The specific system information and the projected orbits are marked correspondingly at the beginning of each row and column. From the top to the bottom row, the results are given in turn for the without pressure and zero band gap pressure systems for the $CaIn_2As_2$, $SrIn_2As_2$, and $BaIn_2As_2$ systems. From the left to the right column, the band projections of the As-s, As-p, In-s, In-p, and AE-d orbitals are shown, and the last column shows their corresponding partial density of states.

transitions compared to Ca(Sr)In_2As_2. The bulk modulus of $AEIn_2As_2$ that we calculated is close to but smaller than $AECd_2As_2$,[22] and they both have the same trends that monotonically decrease across the AE series from Ca to Sr and then to Ba.

It is noteworthy, that we focus on the previously mentioned pressure-induced band gap closure, the projected band structures and their corresponding partial density of states at atmospheric and zero band gap pressures were calculated and the results are presented in six groups in Fig. 4. The occupied states near the Fermi level of the conduction and valence bands are mainly composed of As-s, In-s and As-p, In-p, respectively. We can find that different orbital component of the same element (As or In) undergo band inversion at Γ, such as the In-s orbital is partially distributed in the valence band when it is more distributed in the conduction band, but In-p has the opposite distribution. As shown in the fifth column of Fig. 4, the contribution in the conduction band is more significant when the alkaline earth element is Ba rather than Ca and Sr, which stems from the larger radius and stronger metallicity of

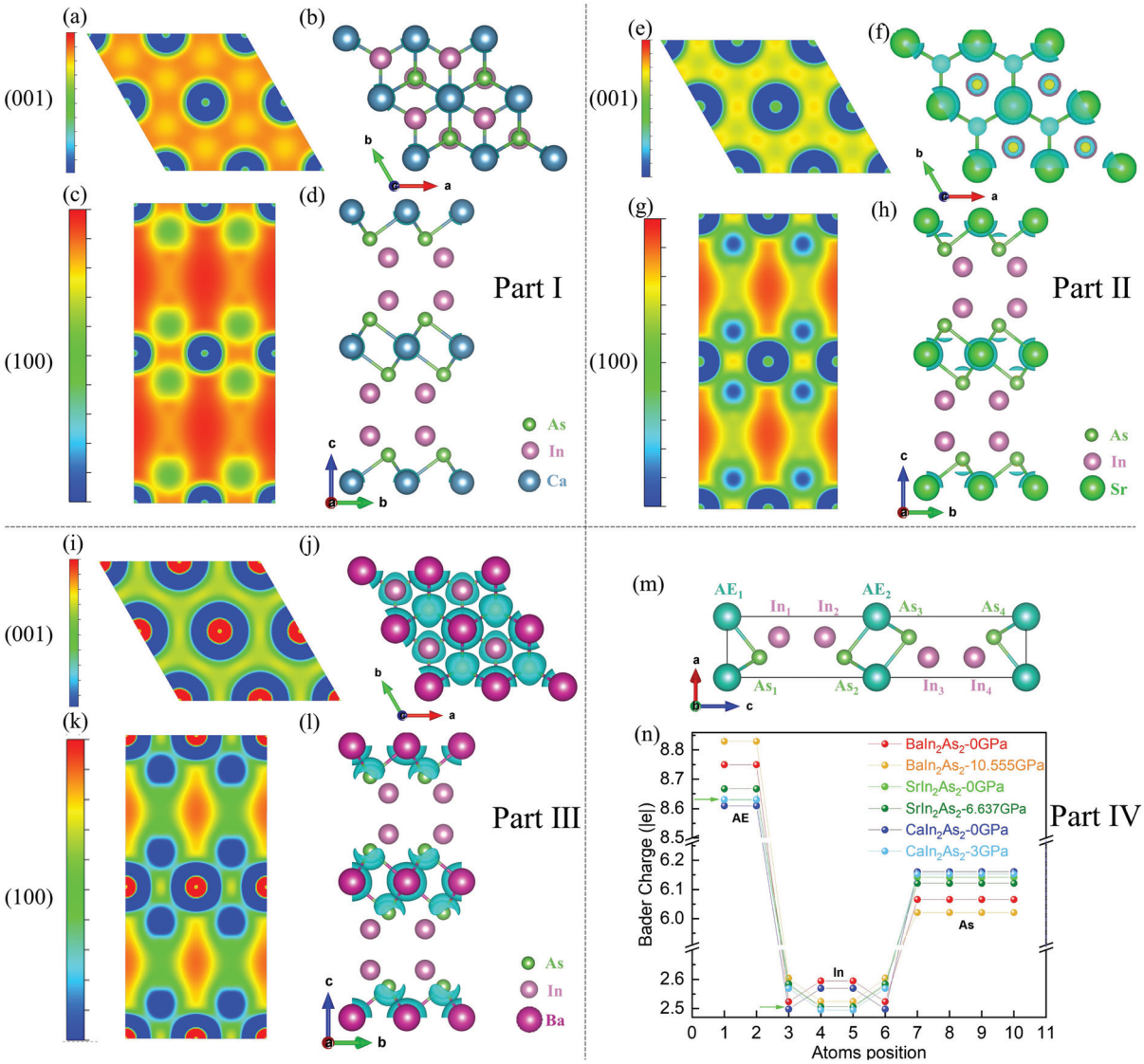

Fig. 5 Differential charge densities between the without pressure and zero band gap pressure systems for the three $AEIn_2As_2$ structures, as well as their Bader Charge calculation results, are separated into four sections by horizontal and vertical dashed lines, where the differential charge densities associated with (a)–(d) $CaIn_2As_2$, (e)–(h) $SrIn_2As_2$, and (i)–(l) $BaIn_2As_2$ are plotted in the upper left, upper right and lower left corners, respectively. The left and right columns of the differential charge density in parts I–III are the two-dimensional and the corresponding three-dimensional form maps for the particular section marked at the beginning of the row, respectively. The differential charge densities were calculated for the (001) and (100) surfaces with a distance from the origin of $0.5 \times d$ and $0 \times d$, and the results were obtained through $2 \times 2 \times 1$ and $1 \times 2 \times 1$ supercells, respectively. The saturation values for all 2D differential charge density plots are shown by the color scale in the figure, increasing equally spaced from a minimum value of −0.007 represented by the blue color to a maximum value of 0 represented by the red color. The isosurface level for all 3D differential charge density is selected to be 0.0106 eV $bohr^{-3}$. The (m) specific atomic occupancies and (n) Bader Charge per atom for the three $AEIn_2As_2$ structures are shown in part IV. The light green arrows in (n) point out where the Bader Charge values for the $SrIn_2As_2$ atmospheric pressure system are overlaid.

Ba. Due to the continuous application of pressure, the electron clouds near the larger radius Ba atoms are more prone to crossover, leading to a drop in the conduction band at M, which is mainly contributed by the d orbital of Ba, as shown in Fig. 4(f5).

3.2 Charge transfer and chemical bonding properties

To clearly reveal the effect of pressure on the electron cloud distribution and charge transfer, we further calculate the differential charge density. As shown in Fig. 5, part I to part III show the differential charge densities between the three $AEIn_2As_2$ structures in the atmospheric pressure system and the zero band gap pressure system according to the AE ion radius from small to large. The differential charge density is defined as $\Delta\rho = \rho_{atmo} - \rho_{zero}$, where ρ_{atmo} and ρ_{zero} represent the charge density of atmospheric pressure and zero band gap pressure systems, respectively. Each of the first three parts contains the two-dimensional and corresponding three-dimensional differential charge density diagrams of the (001) and (100) surfaces. From this phenomenon of charge distribution around the atoms, we can determine that the type of bonding of $AEIn_2As_2$ is typical of ionic bonding. Compared to the zero band gap pressure system, the atmospheric pressure system loses more electrons near the AE and As atoms and appears blue in the differential charge density diagram, which is particularly evident in part III. Because of lattice constant reduction, the application of pressure that induces a zero band gap favors the system to accumulate charge between AE and As atoms while the application of hydrostatic pressure has a negligible effect on the charge distribution near In atoms. Notably, the differential charge density of $BaIn_2As_2$ is more pronounced due to the higher pressure values it needs to induce a zero band gap.

We also analyze the specific charge transfer by Bader charge calculation as shown in Fig. 5(m) and (n). The initial charge numbers of AE, In, and As atoms are 10 $|e|$, 3 $|e|$, and 5 $|e|$, respectively. It shows that AE and In atoms lose electrons to show positive valence while As atoms gain electrons to show negative valence. From the Bader charge curve, it is found that In atoms have two unequal positions different from AE and As that have only one. The equivalent positions of the In atoms satisfy the symmetry of the crystal structure, just as In_2 and In_3 are equivalent. In addition to In_2 and In_3 atoms, other atoms in all three $AEIn_2As_2$ systems show a charge closer to the initial charge value under zero band gap pressure (closer to 10 $|e|$ for AE and 5 $|e|$ for As). And their charge values are closer to the initial charge as the radius of AE atoms increases, indicating that the interatomic bonding of $BaIn_2As_2$ is more unstable, which can be explained by its larger lattice constant.

To compare more clearly the chemical bond strengths of different $AEIn_2As_2$ systems and to observe more quantitatively the effect of pressure on them, we calculated their electron densities and their corresponding Laplacian by AIM analysis. The bond paths between atomic pairs can be determined by the first-order saddle points of electron density. The values of the electron density (ρ_b) and the Laplace of electron density ($\nabla^2\rho_b$) at these points can describe the chemical properties of these bonds.[55,56] The charge densities of bond critical point (3, −1) at the In–In and In–As chemical bonds for different systems are denoted as ρ, see Table 2. As in the results of γ-Si_3N_4 and γ Ge_3N_4,[65] the positive Laplacian values in Table 2 indicate that all In–In and As–In bonds in $AEIn_2As_2$ materials are not typically covalent bonds. In the equivalent case, the As–In bond is stronger than In–In, as can be observed in Table 2. At zero pressure, the ρ_b and $\nabla^2\rho_b$ of In–In in the three Zintl materials are similar while $BaIn_2As_2$ has obviously the lowest value in As–In bonding, which means that the chemical bond is the most unstable, so the conduction band at high pressure falls thus reducing the global band gap of $BaIn_2As_2$. Fig. S3 (ESI†) presents the Laplace isolines for $BaIn_2As_2$ with and without pressure. The chemical bonding is mainly distributed by the purple $\nabla^2\rho_b > 0$, thus indicating that In and In atoms (or As and In atoms) have closed-shell interactions. At 10.555 GPa pressure, the distance between the atoms is reduced, thus enhancing their chemical bond strength. Analysis from another perspective, when the AE elements are the same, applying pressure to induce a zero band gap will all promote the chemical bond strength of As–In and In–In. The strength of all chemical bonds is directly related to the atomic spacing of In–In and As–In, as shown in Fig. S4 (ESI†). Fig. S4 (ESI†) reflects that the In–In bond lengths of the three $AEIn_2As_2$ systems are close at the same pressure, corresponding to the numerical relationship of the electron density ρ_b. And at zero pressure, $BaIn_2As_2$ has the longest In–As bond, so it has the smallest ρ_b in Table 2. For In–In and In–As bond length relationship indicated by pentagons in Fig. S4 (ESI†) is also negatively correlated with the value of ρ_b in Table 2. Therefore, we can assume that the longer similar bond lengths are related to the weaker chemical bond strength.

Under the modulation of the pressure, $AEIn_2As_2$ systems will all achieve an insulator–metal phase transition with a closed band gap and are accompanied by a band inversion. The band gap closure and band inversion are often closely related to the topological properties of the material, so we next discuss the topological properties of $AEIn_2As_2$.

Table 2 The chemical bonding in $AEIn_2As_2$ under special pressure according to the AIM analysis. Both As–In and In–In denote nearest neighbor bonds, and the same bonds exhibit the same properties, for example, In_1–In_2 and In_3–In_4 have the same electron density ρ_b and Laplacian $\nabla^2\rho_b$, so only two bonds, In–As and In–In, are analyzed here

Crystal material		Bond	ρ_b (e bohr^{-3})	$\nabla^2\rho_b$ (e bohr^{-5})
$CaIn_2As_2$	0 GPa	As–In	0.0588	0.0560
		In–In	0.0439	0.1137
	3 GPa	As–In	0.0632	0.0625
		In–In	0.0489	0.1377
$SrIn_2As_2$	0 GPa	As–In	0.0571	0.0543
		In–In	0.0438	0.1140
	6.637 GPa	As–In	0.0660	0.0665
		In–In	0.0543	0.1637
$BaIn_2As_2$	0 GPa	As–In	0.0550	0.0524
		In–In	0.0437	0.1105
	10.555 GPa	As–In	0.0690	0.0681
		In–In	0.0600	0.1884

3.3 Topological quantum phase transition

Aiming to investigate the topological properties of $AEIn_2As_2$ materials, we have performed systematic calculations on the surface states and WCC. It has been theoretically and experimentally reported that the spins of the electrons in the surface state of TIs are highly polarized. And under strong spin–orbit coupling (SOC), the electron spins and crystal momentum are locked together, forming a helical spin texture in the momentum space of the surface states of TIs.[46,63,66–72] Fig. 6 shows the surface state and Fermi surface (FS) in the (001) plane for the $AEIn_2As_2$ system at atmospheric pressure and induced zero band gap pressure. The $AEIn_2As_2$ systems under atmospheric pressure have gapless non-trivial topological surface states and helical spin textures, implying that they belong to strong topological insulators. However, when their band gaps are modulated to zero through the pressure, the edge states of the system near the Fermi level almost disappear and the corresponding spin textures gradually decrease and tend to annihilation. The spin textures of the surface state of $CaIn_2As_2$ on the (001) plane are indicated in green and yellow colors for the 'M'-shaped valence band and the valley conduction band across the Fermi level at the Γ-high symmetry point, respectively. Therefore, it exhibits two spin textures with different directions.

The results for the (010) plane as shown in Fig. S5 (ESI†) similarly indicate the existence of edge states for the system at atmospheric pressure near the Fermi level but essentially absent for all zero band gap pressure systems. Comparing the results in Fig. S5(a), (e), and (i) (ESI†) at atmospheric pressure, we can see that their Fermi levels move across the surface states at different positions, showing a gradual shift from the valence band to the conduction band as the radius of the AE atoms increases.

Furthermore, the spin textures of the $CaIn_2As_2$ system under atmospheric pressure and zero band gap pressure are presented in Fig. S5(b) and (d) (ESI†) are large differences from the $SrIn_2As_2$ and $BaIn_2As_2$ results. As the Fermi levels are shifted, due to without spin texture occlusion, the local enlargements in Fig. S5(a), (e), and (i) (ESI†) show more clearly the variation of the size of the circular Fermi arc openings. With the upward shift of the crossover position between the Fermi level and the surface state, the spin texture is no longer rotated in one direction but undergoes a spin-flip across the center of the circle Fermi arc. As for the results for the surface state at the (001) termination, the surface states on the Γ-high symmetry point near the Fermi level at the (010) termination of the systems under zero band gap pressure vanishes and open a gap, which exhibited a trivial topological physical property, as shown in Fig. S5(c), (g), and (k) (ESI†). The application of high pressure to modulate the $AEIn_2As_2$ systems will lead to a zero band gap but open a gap on the surface state near the Fermi level and thus achieve a quantum topological phase transition.

To confirm that the effect of stress drives the topological phase transition of the $AEIn_2As_2$ systems, we calculated the Wannier Charge Center (WCC), as shown in Fig. 7. At atmospheric pressure (0 GPa), $CaIn_2As_2$, $SrIn_2As_2$, and $BaIn_2As_2$ all exhibit non-trivial topological properties while the topological properties of the systems change to trivial when the pressure modulates band structure to a zero-gap. The $k_x = 0$ and $k_y = 0$ planes exhibit a similar topological situation as the $k_z = 0$ plane. However, we also obtain that the Z_2 topological numbers in the plane where $k_x = 0.5$, $k_y = 0.5$, and $k_z = 0.5$ are zero for all three $AEIn_2As_2$ systems regardless of the atmospheric pressure or zero band gap pressure.

Our studies in the previous two sections induced insulator–metal phase transition and topological quantum phase transition by pressure in $AEIn_2As_2$ systems with the $P6_3/mmc$ space group. In addition to bringing novel topological phase transitions, the

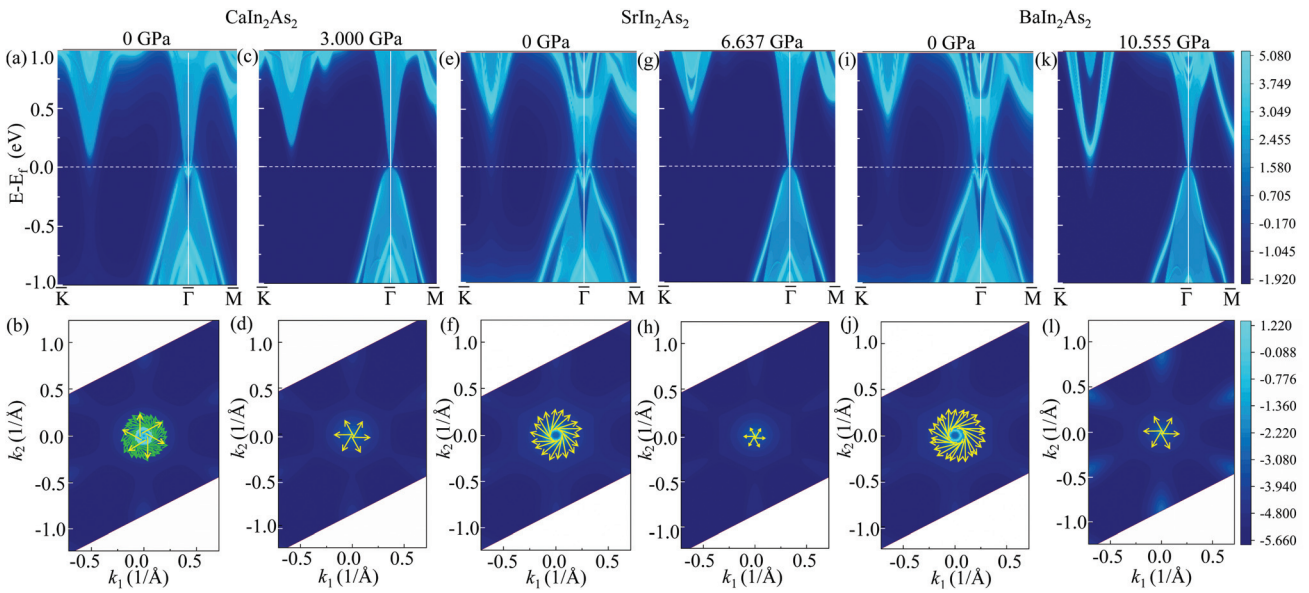

Fig. 6 Surface states of the (001) surface and corresponding Fermi Surfaces (FS) contain spin texture at the Fermi level for the three $AEIn_2As_2$ systems under atmospheric pressure and induced zero band gap pressure. The surface state results for (a)–(d) $CaIn_2As_2$, (e)–(h) $SrIn_2As_2$, and (i)–(l) $BaIn_2As_2$ are marked top of the figure, respectively.

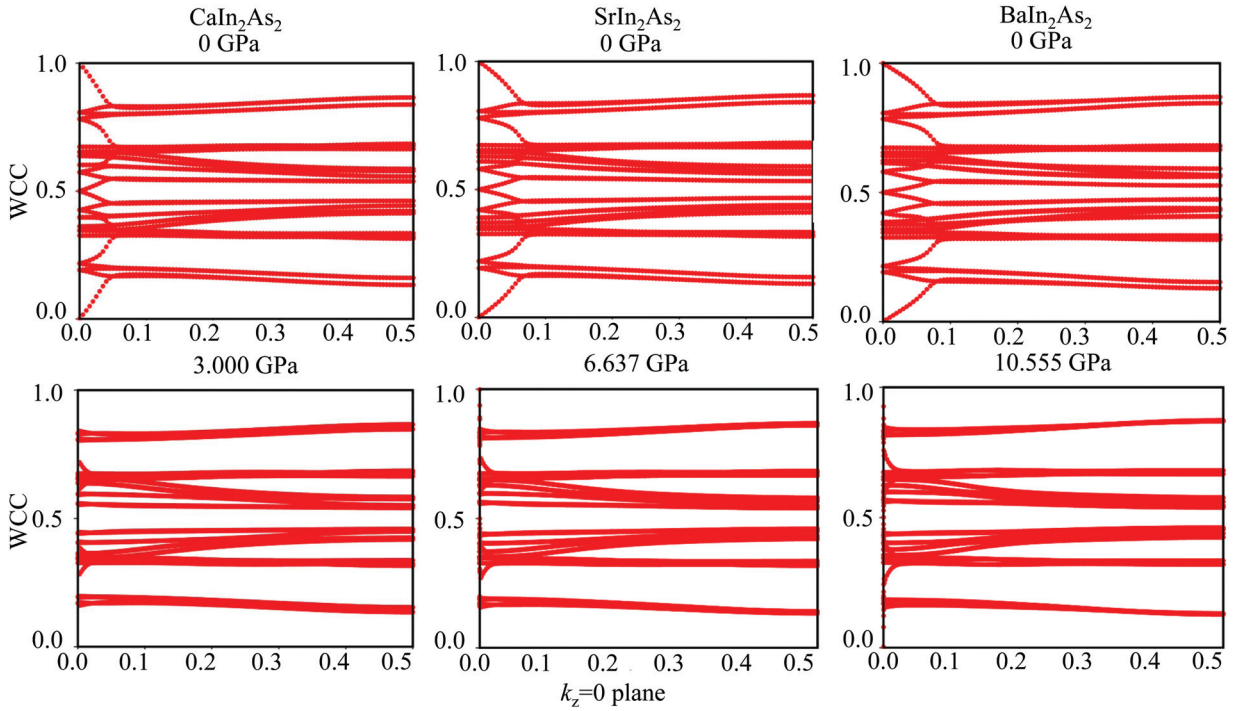

Fig. 7 The Wannier charge center (WCC) on the k_z = 0 plane of $AEIn_2As_2$ systems under the pressures of atmospheric and zero band gap. The system chemical formulas are labeled above each column and the corresponding pressure values are labeled above each image.

application of pressure is usually accompanied by structural phase transitions. We predict from the bulk properties, band gap evolution regulation, and charge transfer under pressure that structural phase transition exists and there are different phase transition characteristics in $AEIn_2As_2$.

4 Conclusions

In conclusion, we have realized the pressure-induced insulator–metal phase transition, topological quantum phase transition in $AEIn_2As_2$ based on first-principles calculations. First, we reveal the pressure-regulated mechanism of $AEIn_2As_2$ undergoing the insulator–metal phase transition. More intriguingly, there are rich and novel topological properties in $AEIn_2As_2$. Next, we reveal the charge transfer and the chemical bonding nature of $AEIn_2As_2$ under pressure. Finally, they will undergo topological quantum phase transition under pressure modulation. Our research has laid an important foundation for both the experimental synthesis and preparation and the further in-depth study of theoretically physical properties of $AEIn_2As_2$ series materials. In addition, it provides feasible new directions for the development of novel topological insulators and spintronic devices for applications.

Author contributions

J.-M. Zhang conceived and supervised this work. W.-T. Guo performed the calculations. W.-T. Guo and J.-M. Zhang wrote the manuscript. Z. Huang analyzed the data and provided valuable and constructive suggestions.

Conflicts of interest

There are no conflicts to declare.

Acknowledgements

We acknowledge the financial support by the National Natural Science Foundation of China (No. 11874113) and the Natural Science Foundation of Fujian Province of China (No. 2020J02018). The work was carried out at the National Supercomputer Center in Tianjin, and the calculations were performed on TianHe-1(A).

References

1 G. Hua, S. Nie, Z. Song, R. Yu, G. Xu and K. Yao, *Phys. Rev. B: Condens. Matter Mater. Phys.*, 2018, **98**, 201116.
2 J. Krishna, T. Nautiyal and T. Maitra, *Phys. Rev. B: Condens. Matter Mater. Phys.*, 2018, **98**, 125110.
3 M. C. Rahn, J.-R. Soh, S. Francoual, L. S. I. Veiga, J. Strempfer, J. Mardegan, D. Y. Yan, Y. F. Guo, Y. G. Shi and A. T. Boothroyd, *Phys. Rev. B: Condens. Matter Mater. Phys.*, 2018, **97**, 214422.
4 C. Niu, N. Mao, X. Hu, B. Huang and Y. Dai, *Phys. Rev. B: Condens. Matter Mater. Phys.*, 2019, **99**, 235119.
5 J.-Z. Ma, S. M. Nie, C. J. Yi, J. Jandke, T. Shang, M. Y. Yao, M. Naamneh, L. Q. Yan, Y. Sun, A. Chikina, V. N. Strocov,

M. Medarde, M. Song, Y.-M. Xiong, G. Xu, W. Wulfhekel, J. Mesot, M. Reticcioli, C. Franchini, C. Mudry, M. Müller, Y. G. Shi, T. Qian, H. Ding and M. Shi, *Sci. Adv.*, 2019, **5**, eaaw4718.

6 J. Ma, H. Wang, S. Nie, C. Yi, Y. Xu, H. Li, J. Jandke, W. Wulfhekel, Y. Huang, D. West, P. Richard, A. Chikina, V. N. Strocov, J. Mesot, H. Weng, S. Zhang, Y. Shi, T. Qian, M. Shi and H. Ding, *Adv. Mater.*, 2020, **32**, 1907565.

7 Y. Xu, Z. Song, Z. Wang, H. Weng and X. Dai, *Phys. Rev. Lett.*, 2019, **122**, 256402.

8 O. Pozo, C. Repellin and A. G. Grushin, *Phys. Rev. Lett.*, 2019, **123**, 247401.

9 T. Sato, Z. Wang, D. Takane, S. Souma, C. Cui, Y. Li, K. Nakayama, T. Kawakami, Y. Kubota, C. Cacho, T. K. Kim, A. Arab, V. N. Strocov, Y. Yao and T. Takahashi, *Phys. Rev. Res.*, 2020, **2**, 033342.

10 S. Regmi, M. M. Hosen, B. Ghosh, B. Singh, G. Dhakal, C. Sims, B. Wang, F. Kabir, K. Dimitri, Y. Liu, A. Agarwal, H. Lin, D. Kaczorowski, A. Bansil and N. Madhab, *Phys. Rev. B: Condens. Matter Mater. Phys.*, 2020, **102**, 165153.

11 S. X. Riberolles, T. V. Trevisan, B. Kuthanazhi, T. Heitmann, F. Ye, D. C. Johnston, S. L. Bud'ko, D. H. Ryan, P. C. Canfield, A. Kreyssig, A. Vishwanath, R. J. McQueeney, L. Wang, P. P. Orth and B. G. Ueland, *Nat. Commun.*, 2021, **12**, 1–7.

12 Y. Zhang, K. Deng, X. Zhang, M. Wang, C. Liu, E. Schwier, S. Kumar, C. Chen and B. Shen, *Bull. Am. Phys. Soc.*, 2020, **65**, 205126.

13 X. Gui, I. Pletikosic, H. Cao, H.-J. Tien, X. Xu, R. Zhong, G. Wang, T.-R. Chang, S. Jia, T. Valla, W. Xie and R. J. Cava, *ACS Cent. Sci.*, 2019, **5**, 900–910.

14 M. Arguilla, N. Cultrara, Z. Baum, S. Jiang, R. Ross and J. Goldberger, *Inorg. Chem. Front.*, 2017, **4**, 378–386.

15 H. Li, S.-Y. Gao, S.-F. Duan, Y.-F. Xu, K.-J. Zhu, S.-J. Tian, J.-C. Gao, W.-H. Fan, Z.-C. Rao, J.-R. Huang, J.-J. Li, D.-Y. Yan, Z.-T. Liu, W.-L. Liu, Y.-B. Huang, Y.-L. Li, Y. Liu, G.-B. Zhang, P. Zhang, T. Kondo, S. Shin, H.-C. Lei, Y.-G. Shi, W.-T. Zhang, H.-M. Weng, T. Qian and D. Hong, *Phys. Rev. X*, 2019, **9**, 041039.

16 L. Zhao, C. Yi, C.-T. Wang, Z. Chi, Y. Yin, X. Ma, J. Dai, P. Yang, B. Yue, J. Cheng, F. Hong, J.-T. Wang, Y. Han, Y. Shi and X. Yu, *Phys. Rev. Lett.*, 2021, **126**, 155701.

17 J.-T. Wang, C. Wang and C. Chen, *Phys. Rev. B: Condens. Matter Mater. Phys.*, 2021, **104**, L220101.

18 M. O. Ogunbunmi, S. Baranets, A. Childs and S. Bobev, *Dalton Trans.*, 2021, **50**, 9173–9184.

19 A. Jain, S. P. Ong, G. Hautier, W. Chen, W. D. Richards, S. Dacek, S. Cholia, D. Gunter, D. Skinner, G. Ceder and K. a Persson, *APL Mater.*, 2013, **1**, 011002.

20 H.-C. Wang, S. Botti and M. A. L. Marques, *npj Comput. Mater.*, 2021, **7**, 12.

21 S. H. Shah, G. Murtaza, A. Baz, E. Algrafy, A. Laref and N. A. Kattan, *Mater. Sci. Semicond. Process.*, 2020, **119**, 105290.

22 J. M. DeStefano and L.-L. Wang, *Phys. Rev. B: Condens. Matter Mater. Phys.*, 2021, **103**, 115207.

23 S. H. Shah, S. Khan, G. Murtaza, M. Amir Ali, A. Laref, E. Algrafy and A. A. H. Ahmadini, *J. Solid State Chem.*, 2020, **292**, 121589.

24 L.-Y. Rong, J.-Z. Ma, S.-M. Nie, Z.-P. Lin, Z.-L. Li, B.-B. Fu, L.-Y. Kong, X.-Z. Zhang, Y.-B. Huang, H.-M. Weng, T. Qian, H. Ding and R.-Z. Tai, *Sci. Rep.*, 2017, **7**, 1–6.

25 K. Shinozaki, Y. Goto, K. Hoshi, R. Kiyama, N. Nakamura, A. Miura, C. Moriyoshi, Y. Kuroiwa, H. Usui and Y. Mizuguchi, *ACS Appl. Energy Mater.*, 2021, **4**, 5155–5164.

26 L. Y. Feng, R. A. B. Villaos, A. B. Maghirang, Z. Q. Huang, C. H. Hsu, H. Lin and F. C. Chuang, *Sci. Rep.*, 2022, **12**, 1–8.

27 M. N. R. Perez, R. A. B. Villaos, L.-Y. Feng, A. B. Maghirang, C.-P. Cheng, Z.-Q. Huang, C.-H. Hsu, A. Bansil and F.-C. Chuang, *Appl. Phys. Rev.*, 2022, **9**, 011410.

28 Y. Ruan, L. Huang, Y. Yang, G. Xu, K. Zhong, Z. Huang and J.-M. Zhang, *Phys. Chem. Chem. Phys.*, 2020, **22**, 3867–3874.

29 C.-Y. Pei, Y.-Y.-Y. Xia, J.-Z. Wu, Y. Zhao, L.-L. Gao, T.-P. Ying, B. Gao, N.-N. Li, W.-G. Yang, D.-Z. Zhang, H.-Y. Gou, Y.-L. Chen, H. Hosono, G. Li and Y.-P. Qi, *Chin. Phys. Lett.*, 2020, **37**, 66401.

30 J. Mutch, W.-C. Chen, P. Went, T. Qian, I. Z. Wilson, A. Andreev, C.-C. Chen and J.-H. Chu, *Sci. Adv.*, 2019, **5**, eaav9771.

31 A. Rancati, N. Pournaghavi, M. F. Islam, A. Debernardi and C. M. Canali, *Phys. Rev. B: Condens. Matter Mater. Phys.*, 2020, **102**, 195110.

32 W.-Z. Zheng, T.-Y. Zhao, A.-Q. Wang, D.-Y. Xu, P.-Z. Xiang, X.-G. Ye and Z.-M. Liao, *Phys. Rev. B: Condens. Matter Mater. Phys.*, 2021, **104**, 155140.

33 Z. Zhang, N. Qi, Y. Wu and Z. Chen, *ACS Appl. Mater. Interfaces*, 2021, **13**, 44409–44417.

34 J. Qu, L. Yan, H. Liu, Q. Tao, P. Zhu, Z. Li and X. Wang, *High Pressure Res.*, 2021, **41**, 318–327.

35 X.-R. Cheng, X.-Y. Kuang, H. Cheng, H. Tian, S.-M. Yang, M. Yu, X.-L. Dou and A.-J. Mao, *RSC Adv.*, 2020, **10**, 12432–12438.

36 P. Liu, G. Zhang, Y. Yan, G. Jia, C. Liu, B. Wang and H. Yin, *Appl. Phys. Lett.*, 2021, **119**, 102403.

37 Z. Shi, W. Shao, L. Rao, X. Xing, Y. Zhou, X. Ren and Q. Yang, *Phys. Chem. Chem. Phys.*, 2022, **24**, 5171–5184.

38 Y. Ruan, Y. Yang, Y. Zhou, L. Huang, G. Xu, K. Zhong, Z. Huang and J.-M. Zhang, *J. Phys.: Condens. Matter*, 2019, **31**, 385501.

39 K. Y. Chen, B. S. Wang, J.-Q. Yan, D. S. Parker, J.-S. Zhou, Y. Uwatoko and J.-G. Cheng, *Phys. Rev. Mater.*, 2019, **3**, 094201.

40 W.-T. Guo, L. Huang, G.-G. Xu, K.-H. Zhong, J.-M. Zhang and Z.-G. Huang, *Acta Phys. Sin.*, 2021, **70**, 047101.

41 Y. Saito, K. Makino, P. Fons, A. V. Kolobov and J. Tominaga, *ACS Appl. Mater. Interfaces*, 2017, **9**, 23918–23925.

42 M. Yang, Y. Z. Luo, M. G. Zeng, L. Shen, Y. H. Lu, J. Zhou, S. J. Wang, I. K. Sou and Y. P. Feng, *Phys. Chem. Chem. Phys.*, 2017, **19**, 29372–29380.

43 C. Q. Xu, R. Sankar, W. Zhou, B. Li, Z. D. Han, B. Qian, J. H. Dai, H. Cui, A. F. Bangura, F. C. Chou and X. Xu, *Phys. Rev. B: Condens. Matter Mater. Phys.*, 2017, **96**, 064528.

44 A. Parveen, E. Narsimha Rao, B. Adivaiah, P. Anees and G. Vaitheüeswaran, *Phys. Chem. Chem. Phys.*, 2018, **20**, 5084–5102.

45 L.-Y. Gan, R. Wang, Y. J. Jin, D. B. Ling, J. Z. Zhao, W. P. Xu, J. F. Liu and H. Xu, *Phys. Chem. Chem. Phys.*, 2017, **19**, 8210–8215.

46 W.-T. Guo, L. Huang, Y. Yang, Z. Huang and J.-M. Zhang, *New J. Phys.*, 2021, **23**, 083030.

47 R. M. Sattigeri, S. B. Pillai, P. K. Jha and B. Chakraborty, *Phys. Chem. Chem. Phys.*, 2020, **22**, 4602–4609.

48 G. Kresse and J. Hafner, *Phys. Rev. B: Condens. Matter Mater. Phys.*, 1993, **48**, 13115–13118.

49 G. Kresse and J. Furthmüller, *Phys. Rev. B: Condens. Matter Mater. Phys.*, 1996, **54**, 11169–11186.

50 P. E. Blöchl, *Phys. Rev. B: Condens. Matter Mater. Phys.*, 1994, **50**, 17953–17979.

51 J. P. Perdew, K. Burke and M. Ernzerhof, *Phys. Rev. Lett.*, 1996, **77**, 3865–3868.

52 J. Heyd, G. E. Scuseria and M. Ernzerhof, *J. Chem. Phys.*, 2003, **118**, 8207–8215.

53 T. D. Kühne, M. Iannuzzi, M. Del Ben, V. V. Rybkin, P. Seewald, F. Stein, T. Laino, R. Z. Khaliullin, O. Schtt, F. Schiffmann, D. Golze, J. Wilhelm, S. Chulkov, M. H. Bani-Hashemian, V. Weber, U. Bortnik, M. Taillefumier, A. S. Jakobovits, A. Lazzaro, H. Pabst, T. Müller, R. Schade, M. Guidon, S. Andermatt, N. Holmberg, G. K. Schenter, A. Hehn, A. Bussy, F. Belleflamme, G. Tabacchi, A. Glöβ, M. Lass, I. Bethune, C. J. Mundy, C. Plessl, M. Watkins, J. VandeVondele, M. Krack and J. u Hutter, *J. Chem. Phys.*, 2020, **152**, 194103.

54 T. Lu and F. Chen, *J. Comput. Chem.*, 2012, **33**, 580–592.

55 R. F. W. Bader, *Chem. Rev.*, 1991, **91**, 893–928.

56 W. Kutzelnigg, *Angew. Chem., Int. Ed. Engl.*, 1993, **32**, 128–129.

57 N. Marzari and D. Vanderbilt, *Phys. Rev. B: Condens. Matter Mater. Phys.*, 1997, **56**, 12847–12865.

58 I. Souza, N. Marzari and D. Vanderbilt, *Phys. Rev. B: Condens. Matter Mater. Phys.*, 2001, **65**, 035109.

59 D. Lee and J. Joannopoulos, *Phys. Rev. B: Condens. Matter Mater. Phys.*, 1981, **23**, 4988.

60 D. Lee and J. Joannopoulos, *Phys. Rev. B: Condens. Matter Mater. Phys.*, 1981, **23**, 4997.

61 M. L. Sancho, J. L. Sancho and J. Rubio, *J. Phys. F: Met. Phys.*, 1984, **14**, 1205.

62 M. L. Sancho, J. L. Sancho, J. L. Sancho and J. Rubio, *J. Phys. F: Met. Phys.*, 1985, **15**, 851.

63 Q. Wu, S. Zhang, H.-F. Song, M. Troyer and A. A. Soluyanov, *Comput. Phys. Commun.*, 2018, **224**, 405–416.

64 F. Birch, *Phys. Rev.*, 1947, **71**, 809–824.

65 P. Mori-Sánchez, M. Marqués, A. Beltrán, J. Jiang, L. Gerward and J. Recio, *Phys. Rev. B: Condens. Matter Mater. Phys.*, 2003, **68**, 064115.

66 J.-M. Zhang, F. Tang, Y.-R. Ruan, Y. Chen, R.-W. Zhang, W.-T. Guo, S.-Y. Chen, J.-P. Li, W. Zhao, W. Zhou, L. Zhang, Z.-D. Han, B. Qian, X.-F. Jiang, Z.-G. Huang, D. Qian and Y. Fang, *J. Mater. Chem. C*, 2021, **9**, 6996–7004.

67 X.-L. Qi and S.-C. Zhang, *Phys. Today*, 2010, **63**, 33–38.

68 J. E. Moore, *Nature*, 2010, **464**, 194–198.

69 O. V. Yazyev, J. E. Moore and S. G. Louie, *Phys. Rev. Lett.*, 2010, **105**, 266806.

70 D. Hsieh, Y. Xia, L. Wray, D. Qian, A. Pal, J. H. Dil, J. Osterwalder, F. Meier, G. Bihlmayer, C. L. Kane, Y. S. Hor, R. J. Cava and M. Z. Hasan, *Science*, 2009, **323**, 919–922.

71 B. Focassio, G. R. Schleder, F. Crasto de Lima, C. Lewenkopf and A. Fazzio, *Phys. Rev. B: Condens. Matter Mater. Phys.*, 2021, **104**, 214206.

72 Z. Xu, M. Ye, J. Li, W. Duan and Y. Xu, *Phys. Rev. B: Condens. Matter Mater. Phys.*, 2022, **105**, 085129.